Molecular Dynamics guided Brownian tomography of apoferritin in liquid water

Silvia Acosta Gutierrez[1,2,‡], **Cesare De Pace**[2,‡], **Gabriel Ing**[2,‡], **Gabriele Marchello**[1,2], **Neil Wilkinson**[3], **Francesco L. Garvasio**[2,4], **Lorena Ruiz Pérez**[1,2,*] and **Giuseppe Battaglia**[1,2,5,*]

[1] *Institute for Bioengineering of Catalonia (IBEC), The Barcelona Institute for Science and Technology (BIST), Barcelona, Spain.*
[2] *Department of Chemistry and Institute of Structural and Molecular Biology, University College London, London, United Kingdom.*
[3] *Gatan UK , Abingdon, UK*
[4] *Department of Pharmaceutical Sciences, University of Geneva, 1211 Geneva, Switzerland*
[5] *Catalan Institution for Research and Advanced Studies (ICREA), Barcelona, Spain*

[*] ***Corresponding authors**: Dr Lorena Ruiz-Perez and Prof Giuseppe Battaglia,Christopher Ingold Building, University College London, 20 Gordon Street, WC1H 0AJ, London, United Kingdom,*
Emails: l.ruiz-perez@ucl.ac.uk and g.battaglia@ucl.ac.uk
[‡] *These authors have contributed equally*

Electron-transparent materials have paved the way for liquid-phase electron microscopy (LPEM), leading to an unprecedented understanding of the structure and dynamics of specimens in their liquid environment. Image reconstruction in liquid-state poses several challenges due to the sample heterogeneity, motion blur, and signal-to-noise ratio in liquid. In this work, we have exploited LPEM to image the dynamics of particles undergoing Brownian motion in confinement, using their sub-diffusional rotation to access the particle conformational ensemble for reconstructing its architecture in 3D using tomographic techniques. We employed tomographic techniques, combining multiple objects into one statistical ensemble or following proteins throughout a video, assessing different conformational states. We guided image reconstruction using molecular dynamics modelling to predict conformational changes. We thus demonstrate we can reconstruct quasi-atomic models with a sub-nanometre spatial resolution of protein structures using apoferritin. We also show that despite achieving a lower spatial resolution than current CryoEM methods, the local resolution of the reconstructed maps via LPEM following a single particle throughout reveals dynamical differences otherwise blurred by combining various particles in a single ensemble

Keywords: liquid phase transmission electron microscopy, protein structure, protein dynamics, apoferritin

1 INTRODUCTION

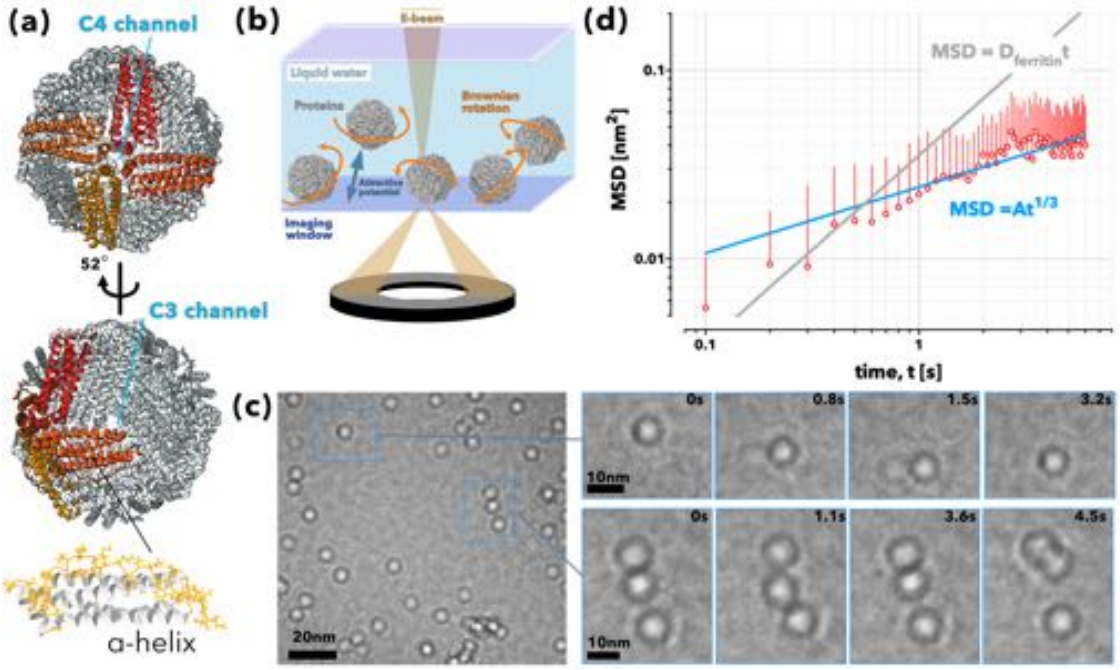

Figure 1: Apoferritin 3D structure (PDBid 6MSX). The apoferritin structure**(a)** is depicted as a cartoon and represented in showing either the C4 or the C3 channel. The secondary structure of the single-chain is shown, highlighting the disordered coils as sticks in orange and α-helices in light grey. Schematics of the experimental set-up **(b)** showing the liquid water entrapped within two silicon nitride windows and the protein able to either diffuse in bulk or interact with the window surface. LPEM micrographs **(c)** showing Apoferritin proteins imaged in liquid water using a K2 direct detection in linear mode, the total movie includes 1200 frames acquired 10 frames/second with 0.1s exposure for each frame. Two regions of interest snapshots at different times show protein dynamics. Apoferritin mean square displacement (MSD) **(d)**)measured as a function of time alongside the theoretical MSD for the protein calculated using a bulk diffusion coefficient $D_{ferritin} = {}^{k_B T}/_{6\pi\eta R}$ where k_B is the Boltzmann constant, $T = 293.16K$ the experiment temperature, $\eta = 1.012Pas^{-1}$ is the water viscosity, and $R = 6nm$ the apoferritin out radius

We chose the apoferritin protein to establish our imaging and analysis methodologies. Apoferritin is a popular cryo-EM benchmark system due to its molecular stability and 24-fold symmetry, which allows high-resolution reconstructions from relatively few particles [1]. The apoferritin has an octahedral shell comprising 24 α–helical subunits with 432-point symmetry (Figure 1a), forming a hollow spherical shell [2] with an external and internal diameter of 12 and 8nm respectively. The three- and four-fold symmetry axes traverse the protein structure across eight C3 and six C4 channels, respectively. The C3 channels emerge from the contact of three different subunit pairs and are circa 2nm in diameter and negatively charged. The C4 channels result from the contact of four other subunit pairs and are narrower than the C3 channels and, to a large extent, hydrophobic [2].

We imaged apoferritin in the liquid phase (Figure S2), obtaining a contrast similar to cryogenic fixation (Figure S2.b) under the same conditions. One current limitation in LPEM is that the faster the imaging, the higher the beam intensity per second to achieve sufficient signal-to-noise. However, the cumulative electron dose needs to be below the damage lethal dose threshold <10 electrons per Å^2 [4]. To maintain the total dose below such a threshold and still achieve sufficient contrast, the fastest we can image proteins is 10fps. Under such experimental conditions, a single apoferritin protein has a translational diffusion coefficient of about 3.4 nms^{-1} well within our temporal resolution. However, apoferritin rotational dynamics has a relaxation time of about 1.4 μs and hence five times faster than our acquisition frequency.

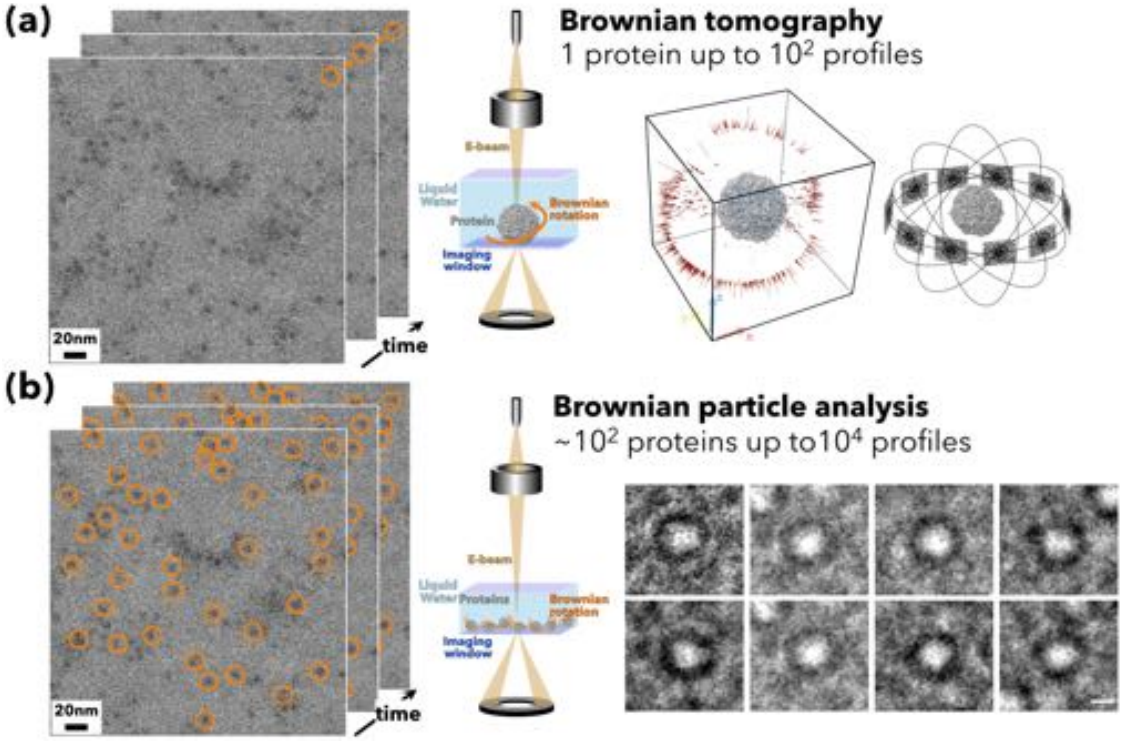

Figure 2: Schematics of the Brownian tomography (**a**) and Brownian particle analysis (**b**) workflows to extract the 3D structure of a protein dispersed in water and undergoing Brownian motion.

A workaround is to image proteins next to the silicon nitride window. While the windows are plasma-treated to increase their wettability, apoferritins will still interact with them and remain entrapped. In Figure 1b), we show the schematics of the imaging geometry, and in Figure 1c) an example of apoferritin particles imaged in liquid water. The regions of interest show that the proteins are mostly bound to the surface with limited diffusion. Yet, such entrapment is relatively soft, and it is common to see proteins unbinding and diffusing out of the field of view. We thus tracked several proteins across different experiments and plotted the resulting mean square displacement (MSD) as a function of time. The data, plotted in Figure 1d) alongside the theoretical MSD, show that apoferritin dynamics are sub-diffusional with an exponent of $1/3$ indicating a strong interaction with the surface yet not sufficiently strong to immobilise the proteins fully. We thus expect that both translation and rotational dynamics are adequately restricted for our imaging conditions, yet as we image them over time, we can still capture different protein orientations. We propose two different approaches to generate 3D reconstructions: Brownian tomography (BT) (Figure 2a) and Brownian particle analysis (BPA) (Figure 2b). Before proceeding with the reconstruction, we applied noise2void neural network-based denoising to the images to increase the signal-to-noise ratio of the video frames [5]. This procedure was required as the signal-to-noise ratio of each dose-fractionation frame was very low due to the low cumulative electron dose used to combat radiation damage. As errors in neural network denoising are random, we predict that any bias in the process will be averaged out in the reconstruction as seen in [6]. In BT, we exploit the rotation of a single particle in the liquid cell to collect different rotational profiles over time, therefore collecting 2D profiles of the same specimen like in ET. In BPA, we considered all the particles in the field of view over time and created a dataset of different profiles. It should be noticed that here the particles experience Brownian motion from one frame to the other at room temperature. Similarly, as in the case of SPA applied to cryo-EM, we obtain/collect different specimen profiles; therefore, a 3D averaged structure of the investigated particle is obtained [7]. This process is iterative and involves an alignment and averaging step to create an initial volume that becomes the reference for the next iteration

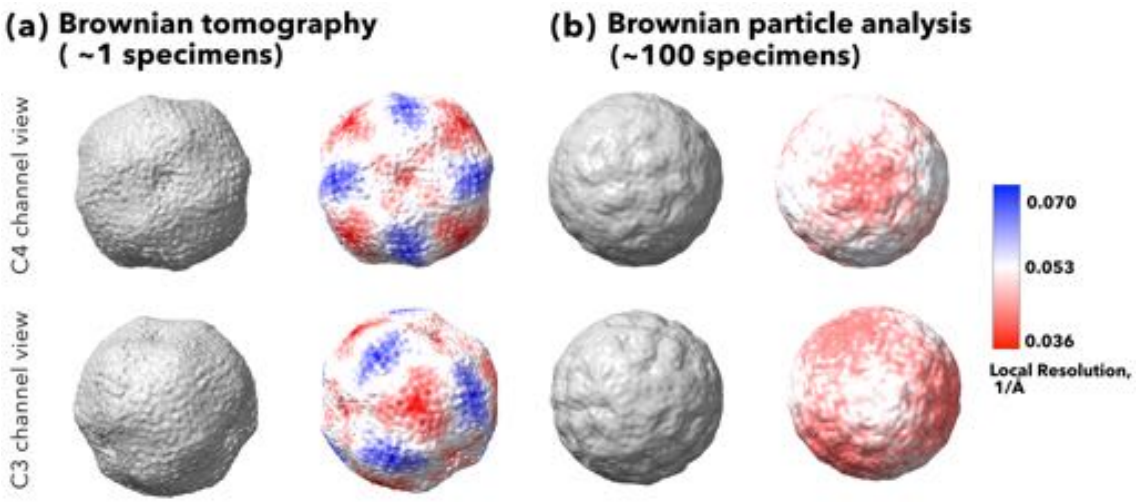

Figure 3: Apoferritin 3D reconstruction from 2D micro-graphs. Apoferritin reconstructed maps from LPEM videos displayed at both C4 and C3 channel orientations as stand-alone density in grey (left-hand side), and coloured according to the filtered local resolution (right-hand side) calculated using the RELION plug-in [3]. The 3D reconstructed structures of apoferritin using LPEM are generated using Brownian tomography (a) and Brownian particle analysis (b).

step. This initial model is further refined through an iterative algorithm, either unbiased or introducing an initial reference model that increases spatial resolution across iterations [8]. Such a reference model should be accurate enough to improve data refinement but not too precise in order not to bias the data. Hence, using a low-pass filtered map of a known similar structure is standard practice. The latter can be either a structure or a sub-structure obtained by other experimental techniques (e.g., x-ray or NMR), computationally generated homology, or even de-novo models. Figure S3 shows the LPEM maps for apoferritin generated using BT and BPA using unbiased refinement. The generated LPEM maps show a spherical structure with indistinguishable features, which do not allow visualising the core-shell structure of apoferritin. The collected 2D profiles from the Brownian rotation of the imaged particles in the liquid sample at room temperature are heterogeneous. Sample heterogeneity is an intrinsic feature of most macro-molecular complexes as part of their dynamic mechanisms of action. Sample heterogeneity poses a difficult challenge for 3D structure determination even in cryoEM, limiting the attainable resolution severely [9] if not addressed. Regions of the structure that display heterogeneous features are incorrectly aligned and averaged with other profiles causing the loss of coherent signal. The ultimate consequence is that areas of the imaged structure with high heterogeneity become blurred or even invisible in the reconstruction, leading to less detailed and incomplete maps. LPEM maps generated with BT and BPA, starting from a low pass-filtered map of 60Å resolution (Figure S4), are shown in Figure 3. The spatial resolution of the maps does not allow us to identify the secondary structure of the single chains. However, other structural factors like the C3 and C4 channels are present in both maps. The calculated resolution at a Fourier Shell Correlation (FSC) value of 0.143 (Figure S5) is very different for both techniques: 20Å and 8Å for the BT and BPA reconstructions, respectively. It must be pointed out that the FSC curves shown in Figure S5 are very noisy due to poor alignment, especially in the BT case. As it happens in cryo-EM, we have no access to the angle and tilt of the profiles, but our specimens are free to move and rotate in-between frames, increasing motion blur. In the BT case, following a single object decreases the number of profiles available for the reconstruction, lowering the resolution of the single reconstructed structure. Nonetheless, reconstructions with similar resolution and a similar number of micro-graphs used for particle selection and reconstruction can be found in the EMDB database from the early 2000s for viral capsids [10, 11], which are nearly ten times larger than apoferritin. We analyzed the local resolution of the obtained maps, Figure3, and observed that in the case of BT reconstruction, there is a difference in the local resolution between the structural elements creating channels and the C3/C4 channels specifically.

In the BPA reconstruction (Figure3b), the local resolution differences among features are lower when compared to BT, and the generated map is more homogeneous. The main difference between both reconstruction methods is the number of profiles accounting for 50 and 2340 in the case of BT and BPA, respectively. These results lead us to conclude that the BPA map is an average of the observed conformations for all specimens, which increases the resolution of the single structure but blurs the dynamical information.

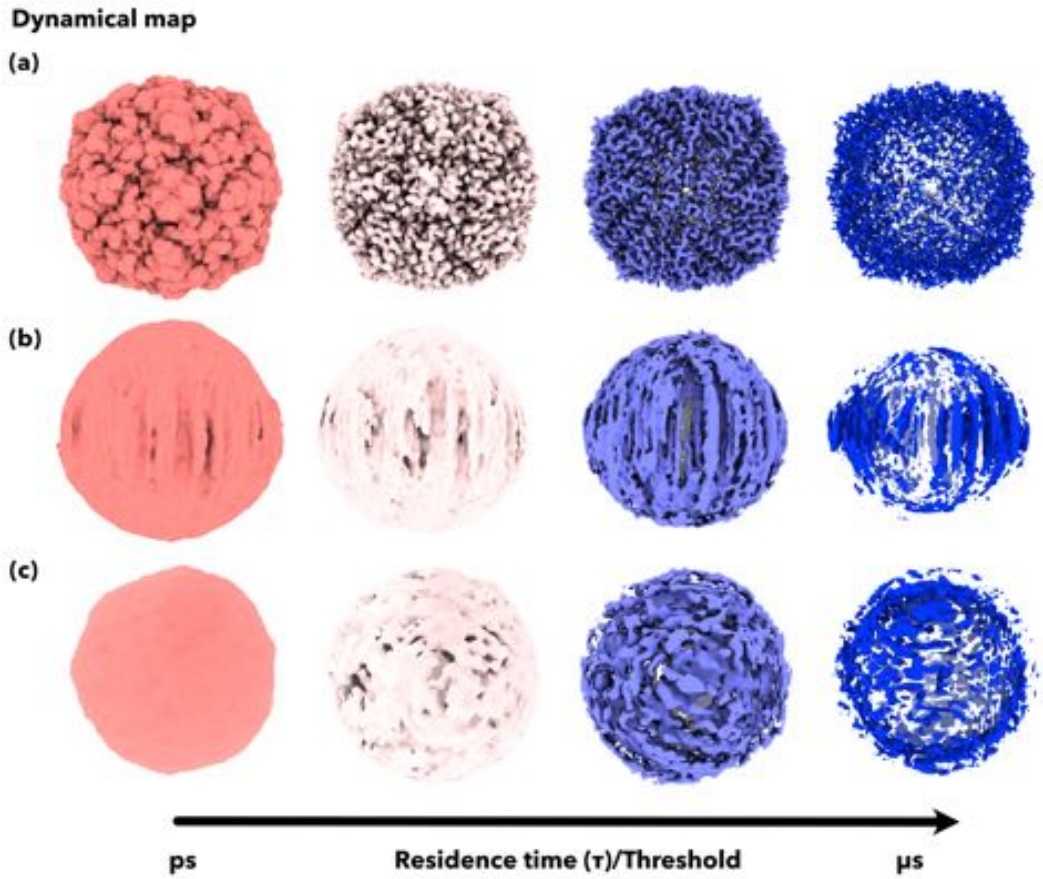

Figure 4: Time evolution of the calculated dynamical map of apoferritin . The calculated dynamical map from a fully aligned and fitted (a), only aligned (b) and only centered (c) trajectories of apoferritin in solution. Maps are depicted and colored at different time thresholds from low (red) to high occupancy (blue).

To understand better the effect of the specimen dynamics or 'sample heterogeneity' on partial occupancy and asymmetric reconstructions we leverage (1μs) molecular dynamics (MD) simulations of apoferritin in solution (150mM NaCl) at room temperature to generate a dynamical map that can be directly compared to our LPEM generated density maps. During the MD simulation, the system under investigation explores the structural ensemble accessible for the starting state at a given temperature. Apoferritin is very stable, and no conformational changes are expected at 300K. We encoded the system fluctuations in what we call the 'dynamical map' by extracting a fourth-dimensional residence time matrix from the all-atom trajectories (Methods). The resulting map for apoferritin is displayed in Figure 4, the different values of the voxels correspond to different atom residency times showing dynamical information at different time scales. The 'dynamical map' encodes thermal fluctuations and the accessible conformational micro-states of the structure at the given temperature. When the trajectory is centred, aligned and fitted (Figure 4a) the obtained map at high residence time resembles those recently obtained for apoferritin at nearly atomic resolution [12, 1, 13], when the trajectory is not fitted (Figure 4b) or not even aligned but only centred (4c), only the shape is retained in the dynamical map.

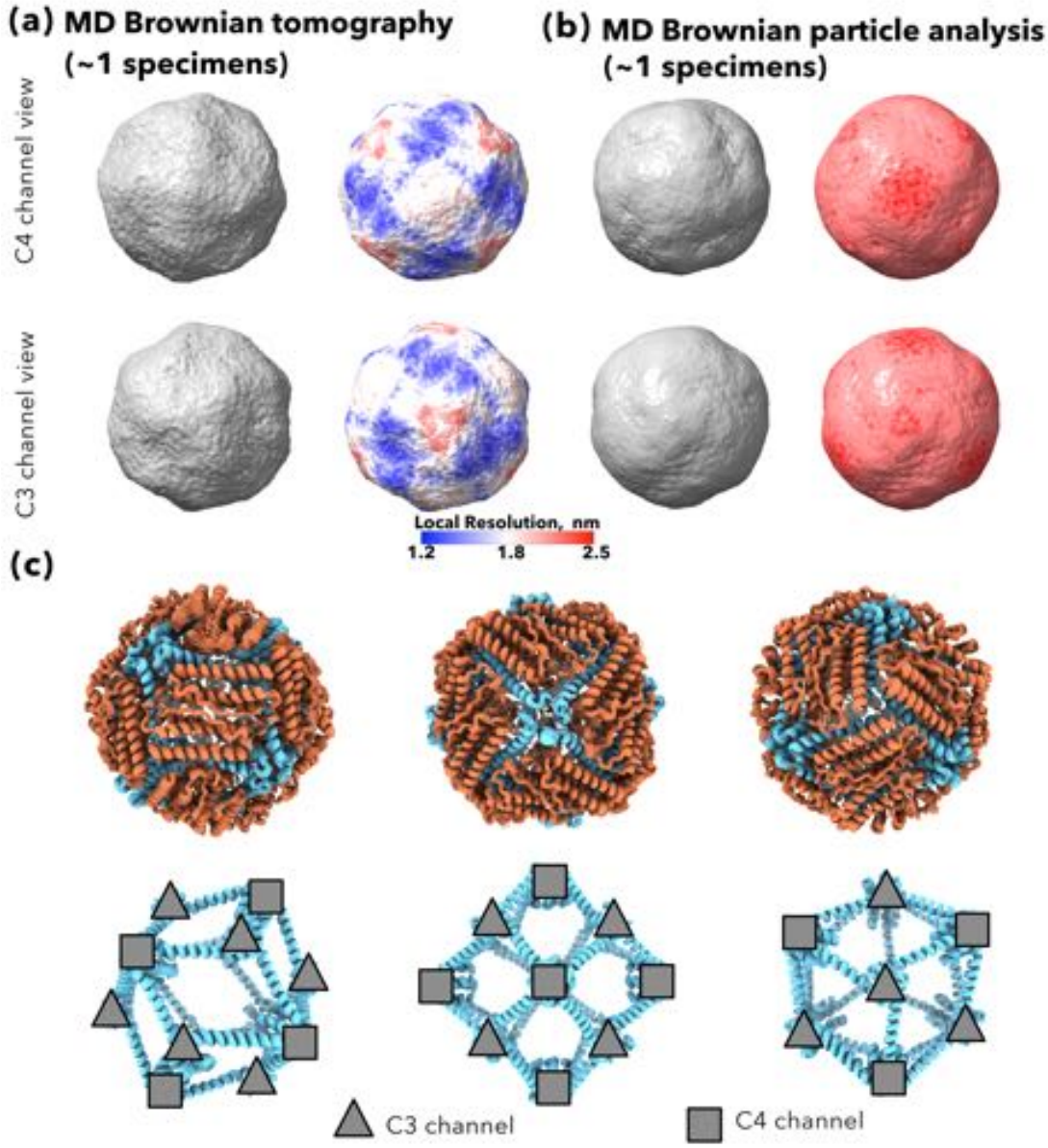

Figure 5: Apoferritin biased 3D reconstruction from 2D micrographs. Apoferritin reconstructed maps from LPEM videos displayed at both C4 and C3 channel orientations as stand-alone density in grey (left-hand side) and colored according to the filtered local resolution (right-hand side) calculated using the RELION plugin [3]. Maps from LPEM are generated with Brownian tomography (a) and Brownian particle analysis (b). One hundred aligned and superimposed snapshots of apoferritin, colored according to the two dynamically distinct regions: the structural elements defining the C3/C4 channels (cyan) and the rest (orange) from the three different profiles that can be distinguished from the symmetry. Below we map onto the most rigid part of the structure (cyan) the location of the C3/C4 channels in the different profiles.

In Figure 5, we show the reconstructed density map using both BT and BPA methods for apoferritin biasing the model refinement with the 'dynamical map' depicted in Figure 4b. The dynamical map includes different conformations of the specimen (when present), while the low-pass-filter map only encodes the fluctuations of a rigid structure. The resolution at 0.143 FSC is unaltered, 20Å in the case of BT and 8Å for BPA. The resolution of the BPA reconstructions varies with the number of unique profiles used in the reconstruction, with an increase in particle number increasing resolution (Fig. S6) . This analysis was done on a random subset of particle

profiles, causing variation in the general trend.Despite the fact that the dynamical map does not seem to improve the calculated spatial resolution, in Figure 5a, the resolution of the map reconstructed employing the BT method looks improved. Both the C3 and C4 channels exhibit lower resolution than the rest of the protein (with and without the dynamical refinement), which correlates with the movement due to the water and ion exchange with the media. We can differentiate two different dynamical regions in the structure (Figure 5c. The structural helices forming the C3/C4 channels, located inside the shell (Figure 5c-cyan), and the helices and coils in between Figure 5c-orange, are located outside. These regions present different average computed b-factors (Figure S7a). The α-helices forming the C3/C4 channels (depicted in cyan) present a lower average b-factor value, 56Å ^{2}, and lower fluctuations (σ =15 Å ^{2}), and this corresponds with the highest density regions in the structure. Conversely, the α-helices and coils (depicted in orange) that are not involved in the formation of the C3/C4 channels have higher flexibility, with an average b-factor of 69Å^2 and fluctuations of 47 Å^2. We have attempted different refinements to test the angular assignment on the overall resolution of the LPEM reconstructed map using BT (Figure S8). We obtained three different maps with resolutions, 34Å, 20Å, and 26Å; as it can be observed in the middle and right panels of Figure S8b, and d, tilt and angle distributions are shifted towards a single value in reconstructions with lower resolution. Currently, many algorithms exist to estimate 2D profiles orientation parameters [14, 15, 16, 17, 18, 19], but the fraction of incorrectly aligned particles can be non-negligible [20, 21]). Unfortunately, the best experimental validation of orientation assignments, tilt-pair analysis, is impossible in liquids, as it requires an immobilised sample, imaged at two different known tilt angles. In liquid-phase, the particles freely rotate making tilt-pair validation impossible. In the case of the BPA reconstructed map, when the dynamical map is used for refinement, Figure 5b, the overall resolution is improved with a value of 8Å. Still, again the local resolution differences observed in the BT reconstruction are blurred. Angles and tilt distributions are broader for all attempted reconstructions (Figure S9). Interestingly, in both cases, the filtered local resolution map always has lower values for the BPA than for the BT reconstructed maps. However, the total spatial resolution is higher for the BPA method. We reconstructed apoferritin particles over time to demonstrate a unique property of LTEM-based BPA reconstruction and evaluate low-resolution electron damage. By selecting the same 49 particles in each frame in the video (example shown in Figure S10a), we could break them up into time-resolved subgroups of 10 frames, with 490 profiles of 49 unique particles per subgroup. These subgroups were then reconstructed individually to give time-resolved reconstructions of 1s (Figure S10b). The resolution of the reconstruction remains relatively constant (Figure S10c), with the final second having a better resolution than the proceeding seconds, demonstrating that there is no significant radiation damage at the low resolutions which we are probing. While at present, this time-resolved BPA can only show that the protein has not fallen apart in the 5s video, in future, this method could show changes in the average structure in solution in response to a change in conditions, for example, the addition of a ligand or change in temperature.

2 CONCLUSIONS

In conclusion, we report a novel way to image proteins in liquid phase exploiting their natural Brownian dynamics to access the proteins' structural ensemble at physiological temperatures. We show that a single protein particle can be followed using the so-called Brownian tomography (BT) method. We can independently reconstruct every particle, compromising on the spatial resolution of the obtained map since single reconstructions are made with fewer profiles. Nevertheless, the loss of spatial resolution when employing the BT method is compensated by the access to dynamical information. The protein dynamics is encoded in the anisotropy on the map and the differences in local resolution. Despite the overall rigidity of apoferritin, we show how the differences in local resolution using the BT method match the dynamics of apoferritin in solution at 300K using molecular dynamics. We also showed that by combining single particle analysis with Brownian dynamics, the so-called Brownian particle Analysis (BPA), we can access more profiles than when using BT; yet, these profiles are shared across several protein units. Hence, the resulting structure is the average conformational space of the investigated proteins. The BPA method yields an improved spatial resolution compared to the BT approach,

but the dynamical differences are not as marked as the BT reconstructed maps. By encoding the conformational space explored during molecular dynamics into the 'dynamical map,' we can sharpen the BT generated maps. Still, the dynamical information is already there even if the LPEM map is reconstructed using a low-pass-filtered map. The role of the dynamical map is not crucial when imaging rigid proteins. Still, we anticipate that the dynamical map will be crucial to reconstructing softer proteins that can undergo significant conformational changes at physiological temperatures. Encoding a sample of the structure possible repertoire will help to unveil the experimentally acquired ensemble. Imaging proteins in liquid state allows us to use Brownian dynamics to capture and assess the different sides of the protein in a fast manner and probe its conformational dynamics. Finally, we can observe that even though our reconstruction does not offer atom-level information, we do image the entire particle. Both inter-and intra-particle dynamics are lost by the need to vitrify the water in cryo-EM or crystallize the proteins in x-ray crystallography, losing important dynamical information usually revealed a posteriori by molecular dynamics. Moreover, it is important to notice that the best cryo-EM reconstructions are based on 10^6 independent particles across a large number of proteins. Our quasi-atomic reconstructions are based on several hundred in BPA and less than a hundred profiles in BT. These numbers of profiles are three and four orders of magnitude less than current cryo-EM approaches, yet we achieve a spatial resolution of about four times worst than that achieved by cryo-EM. Increasing the number of recorded frames per particle and improving the signal-to-noise ratio will soon unveil the 4th dimension in structural biology, accessing important dynamic information that has been out of reach.

3 MATERIALS AND METHODS

Protein sources and production

Equine spleen apoferritin was purchased from Merck (previously Sigma-Aldrich) and diluted with phosphate buffer solution (PBS) at a 1.5 mg/ml concentration. PBS was used instead of water in an attempt to minimize water hydrolysis and radical formation. These two effects are not uncommon when aqueous solutions are placed under high voltage electron beams.

Liquid holder methodology

The liquid holder used for imaging the apoferritin in solution was the Ocean holder from DENSsolution. The sample was sandwiched into a liquid cell formed by two SiN rectangular chips.

The chips were separated by a 200nm spacer. Each chip had a 50nm-thick silicon nitride electron transparent observing window of dimensions 50 μm x 200 μm placed geometrically in the centre of the chips. First, the chips were cleaned with HPLC-graded acetone followed by isopropanol for 5 minutes each, to remove their protective layer made of poly(methyl methacrylate). Then, the chips were plasma cleaned for 13 minutes to further clean them, increase their hydrophilicity and allow better specimen wettability. The chips were then inserted onto the liquid cell placing the chip with the spacer at the bottom, where 1.5 μL of ferritin solution at 1.5 mg/mL was casted. It was important not to allow the ferritin solution to dry at this stage as the film thickness generated by the dried ferritin solution cannot be easily controlled and impedes good imaging conditions. The chip without any spacer was placed at the top enclosing the liquid cell. It is possible to position the chips in different conformation: parallel or crossed (Figure S12). The parallel position allows a larger viewing area, but the windows are more likely to break during liquid cell assembly and they may be misaligned due to a mechanical shift during liquid cell assembly. The crossed or perpendicular position however generally provides a smaller viewing area than the parallel configuration, but it allows consistency in the experiments as it is always possible to find an area for the imaging. Hence, the observing windows at the top and bottom chips were placed in a perpendicular configuration.

An important variable in the liquid cell setting is the liquid thickness, which will directly affect the electrons transmitted through the specimen.

The liquid holder was sealed, and 300 μL of the ferritin solution at 1.5 mg/mL was flushed in at 20 µL/min with a peristaltic pump. A volume of 300 μL of solution ensured that the holder

tubing system and cell were filled with ferritin solution. Although the liquid thickness is dictated by the spacer used in the liquid cell, the observation windows of the SiN chips tend to experience some bulging, mainly at their center point. This bulging effect is due to the differential pressure encountered by the holder once it is inserted into the vacuum of the microscope. The bulging phenomenon of the windows adds some extra thickness to the observation chamber. This effect is well documented in the literature [22, 23] and must not be underestimated. Indeed media thickness is of crucial importance as thick samples tend to acquire more inelastic scattering leading to radiation damage and low resolution.

In order to image at the most optimal positions within the viewing windows i.e. reduced thickness , we performed Electron Energy loss spectroscopy (EELS) thickness measurements to assess the inelastic water scattering (see Fig.S12). Such analysis allowed us to identify the areas with reduced liquid thickness and reduced inelastic scattering. The repeatability of the membrane location allowed us to build a thickness list that was common to every position of the viewing window when inserting the holder. Using EFTEM Thickness, we could indeed map out the bowing of the SiN observing windows via a montage of thickness maps. This approach allowed for a precise measurement/calculation of media thickness in later images. In the Ocean holder configuration, we found thick water layers to be consistently present in the central viewing region which results in a dark area when imaging it because the electrons are not transmitted efficiently. Conversely the corners of the viewing window show much brighter areas due to reduced bulging and thin water layers (Fig.S11). This pattern of dark and bright areas at low mag also serves to verify the presence of liquid in the liquid cell as it mirrors the water layer thickness. In the event of no liquid being present in the liquid cell the pattern of dark and bright areas is not present as the electrons are transmitted efficiently through air. For the imaging experiment presented herein, the liquid layer should be as thin as possible to be able to gather good contrast in the imaged particle profiles and achieve a SNR high enough to allow for structure reconstruction. Higher SNR also implies that electron doses can be kept low allowing for the best resolution that can be achieved. All the videos and data presented herein have been acquired at the reduced thickness areas located at the corners of the viewing window.

Imaging was performed with the holder in static conditions, i.e., the pumps were stopped during imaging. Fluid dynamics simulations were performed on the OCEAN liquid holder and are reported in the SI section.

Imaging methodology

The experiments were performed using a JEOL JEM-2200FS TEM microscope equipped with a field emission gun (FEG) at 200 kV and an in-column Omega filter. The camera used was the direct detection device (DDD) K2-IS camera from Gatan. The ultra-high sensitivity of the K2 allows low-dose imaging modes to limit electron dose damage considerably and facilitate high spatial (3838×3710 pixels) and temporal (up to 1600 fps in in-situ mode) resolution. The microscope was used in transmission electron microscopy mode i.e. parallel beam illumination . In order to limit the beam dose on the specimen, images were collected at the minimum spot size (5) with a small condenser lens aperture (CLA 2). The K2 can be used in two recording modes, linear and counted. The former is fast, but it generates the output image by capturing the integrated signal from each pixel, similar to a standard charge-coupled device (CCD). Counted mode processes the image and assigns one count to the pixel or sub-pixel of the landing site of that electron. For our investigations, dose fractionation videos were recorded in counted mode. Further details on the quality of the videos are provided in the Video analysis section. The apoferritin video used was a single 5s dose fractionation video at 10fps, resulting in 50 frames. The electron flux was circa 0.09 e-/Å2 per frame and a total cumulative electron dose of 4.5e-/Å2, this gives a total electron dose per particle of approximately 1270000 e-/particle across the 5s imaging time. The magnification used for apoferritin was 20Kx.

The present investigations on proteins in liquid, unfortunately, occurs with time resolution slower than the object rotational relaxation times. Without going into complex geometrical consideration to calculate the rotational dynamics of the ferritin structure approximating it to spherical geometry for simplicity, i.e ., a sphere of diameter 12nm , will change orientation every approx. 10-5 s, 3 orders of magnitude faster than the speed at which we can image. While we are not able to track rotational dynamics with our current set-up, we can still use the

consequent randomization of the object to capture enough profiles to feed our tomographic algorithms. Hence we have not discussed the speed of rotation of the proteins and whether the object is located on an interfacial layer, area with slow movement, or at the bulk with regards to its speed of rotation. Along the same lines we have not discussed whether what is observed is special/peculiar, or if the speed of the imaged proteins is what a general model would predict. This analysis is outside of the scope of the present investigation. We have however provided an analysis of the areas with reduced thickness where the imaging have been performed.

Molecular dynamics

We simulate apoferritin starting from the biological assembly of a 1.43Å resolution x-ray crystal structure (PDB-id: 6MSX) containing Cd2+. Only the positions of the protein coordinated Cd2+ atoms were retained and simulated as Fe2+. The protein complex presented no mutations or structural gaps; therefore, it was protonated at pH 7.4 and solvated (150mM NaCl) using a TIP3P[24] water model and Charmm36m [25] protein and ions force field. The final simulated system consisted of 336806 atoms, resulting in a truncated octahedron simulation cell of 16.14nmx15.21nmx13.17nm (5.37, -5.37,7.6). All simulations were performed with Gromacs v2019.2 [26] with a 2fs integration step. We performed 2000 steps of minimization (steepest descent algorithm), followed by 5000 steps of isotropic NPT at 300K, using the velocity-rescaling thermostat[27] and Parrinello-Rahman barostat [28]. After 50000 steps of NVT the system was fully equilibrated and ready for production, which was performed in the NVT ensemble for 1 microsecond.

Dynamical map calculation

We calculated a fourth-dimensional residence time matrix for apoferritin, from its all-atom MD trajectories. For each frame of the trajectory, the system is roto-translated into a template (initial molecular dynamics structure). The rotation matrix of the system snapshot onto the template is calculated using a least-squares rigid motion transformation using single value decomposition. Then an occupation fourth-dimensional matrix is calculated and exported as a volumetric map.

Reconstruction methodology

The individual frames of the dose-fractionation videos were exported and processed individually. The apoferritin frames were first denoised using a noise2void neural network [5], with a network trained on sets of 200 similar apoferritin video frames. Reconstructions were performed using Relion 2.0 methods [3] within the Scipion framework [29]. For Brownian tomography, the particles were tracked and picked manually across the consecutive frames to render 50 profiles per particle for apoferritin. For apoferritin, many particles within each frame were manually picked, rendering a total of 2340 profiles. To create the plot shown in Figure S6, random groups of profiles were selected from the 2340 profiles using a custom python script to edit the particles.star files. The time-resolved structures for apoferritin used profiles of 49 particles across the 10 frame (1s) intervals, making 490 profiles per reconstruction. The particle sets were then used with *relion refine* to refine models of the respective protein, with initial models originating either from atomic models low-pass filtered to 60Å or from dynamic models representing the residence time of atoms from a 1μs long simulation of the proteins. Octahedral symmetry was applied for ferritin refinement.

4 ACKNOWLEDGEMENT

We thanks Prof Finn Werner and Dr Simona Pilotto from the Institute of Structural and Molecular Biology at University College London for the valuable feedbacks

5 FUNDING

We acknowledge the EPSRC (grant EP/N010906/1) , Jeol UK and DENSsolutions for sponsoring part of this work, LRP salary as well as GM and CDP scholarship. GB acknowledges the EPSRC for funding part of his salary via an Established Career Fellowship (EP/N026322/1) and the ERC (CheSSTag 769798) via a consolidator award F.L.G. acknowledges funding from EPSCR (Grants EP/P022138/1, EP/P011306/1) and European Commission H2020 Human Brain Project CDP 6. HEC-BioSim (EP/R029407/1), PRACE (BSC, Project BCV-2019-3-0010 and CSCS ProjectS847), CSCS (Project 86), and the Leibniz Supercomputing Center (SuperMUC, Project pr74su) are acknowledged for their generous allocation of supercomputer time. G.B. and S.A.G. acknowledge the Spanish Supercomputer Network, RES, for their allocation of HPC resources, project BCV-2020-3-0009 (Tirant UV). GI acknowledges the Wellcome Trust for funding his studentship (222908/Z/21/Z).

References

[1] T. Nakane, A. Kotecha, A. Sente, G. McMullan, S. Masiulis, Pmge Brown, I. T. Grigoras, L. Malinauskaite, T. Malinauskas, J. Miehling, T. Uchanski, L. Yu, D. Karia, E. V. Pechnikova, E. de Jong, J. Keizer, M. Bischoff, J. McCormack, P. Tiemeijer, S. W. Hardwick, D. Y. Chirgadze, G. Murshudov, A. R. Aricescu, and S. H. W. Scheres. Single-particle cryo-em at atomic resolution. *Nature*, 587(7832):152–156, 2020.

[2] E. C. Theil. Ferritin: structure, gene regulation, and cellular function in animals, plants, and microorganisms. *Annu Rev Biochem*, 56:289–315, 1987.

[3] Faster to a structure with relion-2. *Nature Methods*, 14(1):12–12, 2017.

[4] Joachim Frank. Single-particle reconstruction of biological macromolecules in electron microscopy–30 years. *Quarterly reviews of biophysics*, 42(3):139–158, 2009.

[5] Alexander Krull, Tim-Oliver Buchholz, and Florian Jug. Noise2void-learning denoising from single noisy images. In *Proceedings of the IEEE/CVF Conference on Computer Vision and Pattern Recognition*, pages 2129–2137.

[6] Tristan Bepler, Kotaro Kelley, Alex J. Noble, and Bonnie Berger. Topaz-denoise: general deep denoising models for cryoem and cryoet. *Nature Communications*, 11.

[7] S. Jonic, C. O. Sorzano, and N. Boisset. Comparison of single-particle analysis and electron tomography approaches: an overview. *J Microsc*, 232(3):562–79, 2008.

[8] Kendra E. Leigh, Paula P. Navarro, Stefano Scaramuzza, Wenbo Chen, Yingyi Zhang, Daniel Castaño-Díez, and Misha Kudryashev. *Subtomogram averaging from cryo-electron tomograms*, pages 217–259. Methods in Cell Biology. 2019.

[9] R. Henderson, S. Chen, J. Z. Chen, N. Grigorieff, L. A. Passmore, L. Ciccarelli, J. L. Rubinstein, R. A. Crowther, P. L. Stewart, and P. B. Rosenthal. Tilt-pair analysis of images from a range of different specimens in single-particle electron cryomicroscopy. *J Mol Biol*, 413(5):1028–46, 2011.

[10] Carmen San Martin, Roger M. Brunette, Felix de Haas, Ralph Heinkel, Twan Rutten, Stephen D. Fuller, Sarah J. Butcher, and Dennis H. Bamford. Combined em/x-ray imaging yields a quasi-atomic model of the adenovirus-related bacteriophage prd1 and shows key capsid and membrane interactions. *Structure*, 9:917–930, 2001.

[11] Carmen San Martin, Juha T. Huiskonen, Jaana K.H. Bamford, Sarah J. Butcher, Stephen D. Fuller, Dennis H. Bamford, and Roger M. Burnett. Minor proteins, mobile arms and membrane-capsid interactions in the bacteriophage prd1 capsid. *Nature Structure Biology*, 9:756–63, 2002.

[12] K. Naydenova, P. Jia, and C. J. Russo. Cryo-em with sub-1 a specimen movement. *Science*, 370(6513):223–226, 2020.

[13] K. M. Yip, N. Fischer, E. Paknia, A. Chari, and H. Stark. Atomic-resolution protein structure determination by cryo-em. *Nature*, 587(7832):157–161, 2020.

[14] Sjors H.W. Scheres. A bayesian view on cryo-em structure determination. *Journal of molecular biology*, 415(2):406–418, 2012.

[15] C. O. S. Sorzano, J. Vargas, J.M. de la Rosa-Trevín, J. Otón, A. Alvarez Cabrera, V. Abrishami, E. Sesmero, R. Marabini, and J.M. Carazo. A statistical approach to the initial volume problem in single particle analysis by electron microscopy. *Journal of Structural Biology*, 189:213–219, 2015.

[16] A. Punjani, M.A. Brubaker, and D.J. Fleet. Building proteins in a day: Efficient 3d molecular structure estimation with electron cryomicroscopy. *IEE Transactions on Pattern Analysis and Machine Intelligence*, 39:706–718, 2017.

[17] T. Grant, A. Rohou, and N. Grigoreff. cistem, user-friendly software for single-particle image processing. *eLife*, 7:e35383, 2018.

[18] C.F. Reboul, M. Eager, D. Elmlund, and H. Elmlund. Single-particle cryo-em-improved ab initio 3d reconstruction with simple/prime. *Protein Science*, 27:51–61, 2018.

[19] C. O. S. Sorzano, J. Vargas, J.M. de la Rosa-Trevín, A. Jimenez, D. Maluenda, R. Melero, M. Martinez, E. Ramirez-Aportela, P. Conesa, J.L. Vilas, R. Marabini, and J.M. Carazo. A new algorithm for high-resolution reconstruction of single particles by electron microscopy. *Journal of Structural Biology*, 204:329–337, 2018.

[20] J. Vargas, J. Oton, R. Marabini, J.M. Carazo, and C.O.S. Sorzano. Particle alignment reliability in single particle electron cryomicroscopy: A general approach. *Scientific Reports*, 6:21626, 2016.

[21] J. Vargas, R. Melero, J. Gomez-Blanco, J.M. Carazo, and C.O.S. Sorzano. Qualitative analysis of 3d alignment quality: Its impact on soft-validation, particle pruning and homogeinity analysis. *Scientific Reports*, 7:6307, 2017.

[22] Hanglong Wu, Hao Su, Rick R. M. Joosten, Arthur D. A. Keizer, Laura S. van Hazendonk, Maarten J. M. Wirix, Joseph P. Patterson, Jozua Laven, Gijsbertus de With, and Heiner Friedrich. Mapping and controlling liquid layer thickness in liquid-phase (scanning) transmission electron microscopy. *Small Methods*, 5:e2001287, 2021.

[23] Nestor J. Zaluzec, M. Grace Burke, Sarah J. Haigh, and Matthew A. Kulzick. X-ray energy-dispersive spectrometry during in situ liquid cell studies using an analytical electron microscope. *Microscopy and Microanalysis*, 20:323–329, 2014.

[24] William L. Jorgensen, Jayaraman Chandrasekhar, Jeffry D. Madura, Roger W. Impey, and Michael L. Klein. Comparison of simple potential functions for simulating liquid water. *The Journal of Chemical Physics*, 79(2):926–935, 1983.

[25] J. Huang, S. Rauscher, G. Nawrocki, T. Ran, M. Feig, B. L. de Groot, H. Grubmuller, and Jr. MacKerell, A. D. Charmm36m: an improved force field for folded and intrinsically disordered proteins. *Nat Methods*, 14(1):71–73, 2017.

[26] Mark James Abraham, Teemu Murtola, Roland Schulz, Szilárd Páll, Jeremy C. Smith, Berk Hess, and Erik Lindahl. Gromacs: High performance molecular simulations through multi-level parallelism from laptops to supercomputers. *SoftwareX*, 1-2:19–25, 2015.

[27] G. Bussi, D. Donadio, and M. Parrinello. Canonical sampling through velocity rescaling. *Journal of Chemical Physics*, 126:014101, 2007.

[28] A. Rahman and M. Parrinello. Polimorphic transitions in single crystals: A new molecular dynamics method. *Journal of Applied Physics*, 52:7182, 1981.

[29] J. M. de la Rosa-Trevín, A. Quintana, L. del Cano, A. Zaldívar, I. Foche, J. Gutiérrez, J. Gómez-Blanco, J. Burguet-Castell, J. Cuenca-Alba, V. Abrishami, J. Vargas, J. Otón, G. Sharov, J. L. Vilas, J. Navas, P. Conesa, M. Kazemi, R. Marabini, C. O. S. Sorzano, and J. M. Carazo. Scipion: A software framework toward integration, reproducibility and validation in 3d electron microscopy. *Journal of Structural Biology*, 195(1):93–99, 2016.

6 SUPPORTING INFORMATION

Fluid dynamics simulation

The section about the liquid cell preparation and assembly shows how demanding this technique can be, and it is not surprising that the first attempts to image proteins in liquid state failed due the high complexity of the system . Therefore, a fluid dynamics simulation was performed by using COMSOL Multi-physics in order to understand the fluid dynamics performance of the holder and liquid cell when the inlet and outlet tubing systems where employed in-flow conditions. The Ocean liquid holder was modelled in COMSOL using the actual dimensions of the device, the values of which will not be reported in this paper so as not to violate the confidentiality agreement signed between the authors and the manufacturing company. However, the simplified geometry of the holder is shown in **fig:FIGS1**a. The tip of the holder is flower-shaped and is connected to two in-plane parallel pipes, an inlet and outlet pipe for flowing in and out of the solution respectively. The holder hosts on the inside two SiN chips separated by a variable gap, creating a microfluidic channel to enable inflow analysis and keep the sample hydrated. The bulging effect on the observation windows occurring when imaging the sample and mentioned in section covering the liquid cell preparation and assembly has been excluded from the simulation. This is because the simulation has been performed at atmospheric pressure conditions, i.e. when the liquid sample is flowed in the liquid holder when the holder is placed outside the microscope. Thus, the windows are treated as flat, rigid surfaces trapping the solution on the inside. Input and output ports were set to the end of the pipes, guaranteeing good fluid circulation. At the beginning of the simulation the chamber was modelled as empty, both chips were removed, and an uncompressible Newtonian fluid was pumped in with an initial velocity of 5 μL/min. The analysis was performed at steady state, imposing laminar flow, planar symmetry and no slip condition on the walls of the holder. The velocity of the fluid in these conditions was analyzed and the results are reported in **fig:FIGS1**b. This first preliminary simulation was mainly performed to validate the goodness of the model, and especially to analyze the trajectory of the flow. The first simulation confirmed that the fluid linearly went from the inlet to the outlet pipes, slowly expanding in the whole volume of the chamber. The results showed that the trajectory of the injected particles was a combination of both convection and Brownian motion experienced by nanoparticles in liquid. Then the complexity of the system was increased by adding the two chips inside the flower-shaped tip, separated by a 200nm spacer. The inclusion of the chips significantly influenced the liquid flow inside the chamber, modifying the liquid trajectory and narrowing it down to the small microfluidic channel between the chips. Consequently, most of the fluid went into the petals of the structure, generating a turbulent flow. Furthermore, the volume between the two chips was filled with only a small portion of the incoming fluid, the motion of which was hardly moved by the effect of the pump (Fig. S1c). In a first approximation model, these results can be extended to the particles in solution pumped in the inflow port; mirroring the actual experimental conditions. As a consequence, most of the particles would not flow between the observation window, but instead be trapped in the flower petal reservoir. These findings strongly suggest that parameters such as sample concentration and velocity at which the sample is injected into the holder have to be carefully chosen, in order to maximize the number of the particles in the viewing window area.

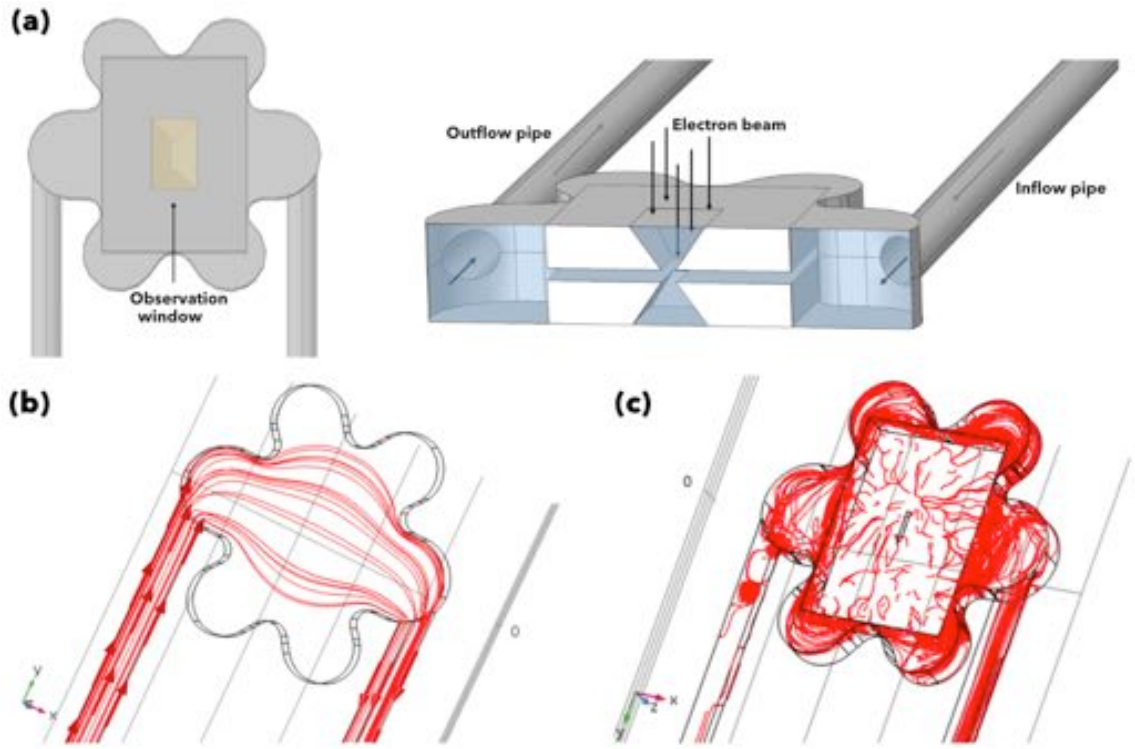

Figure S1: Liquid cell holder. Schematics of the liquid holder used for imaging liquid sample by transmission electron microscopy (a). Fluid dynamics simulations of the holder, modelled without the SiN chips (b). A Newtonian fluid was pumped in the inflow pipe (on the left) and out from the outflow pipe (on the right). The flow expands towards the flower shape reservoir perpendicular to the liquid main trajectory while flowing through the chamber. Fluid dynamics simulations of the holder comprising two chips inside (c). Both simulations run applying laminar flow, planar symmetry and no slip conditions; the analysis was then performed at steady state.

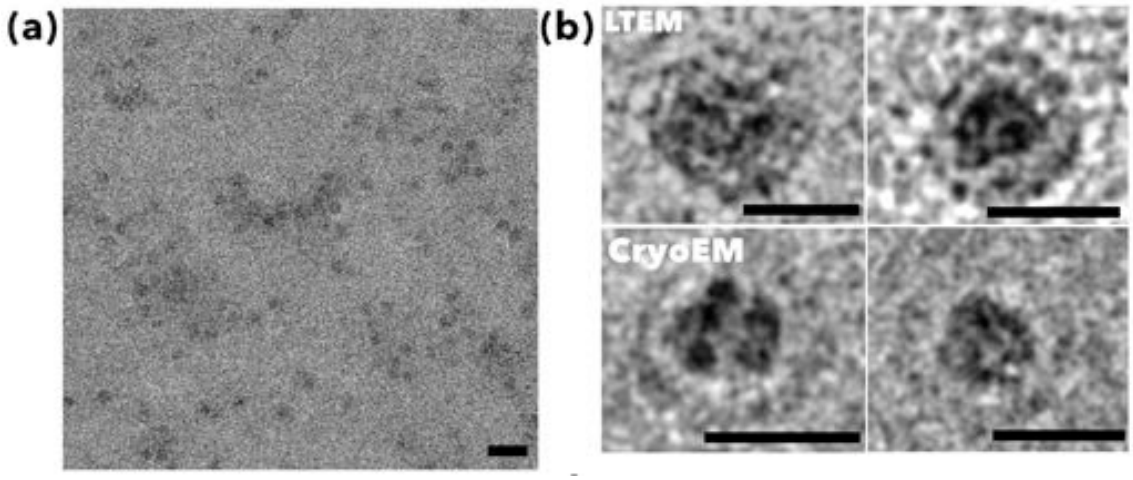

Figure S2: Liquid phase transmission electron microscopy (LPEM) imaging of proteins. LPEM micro-graphs of apoferritin particles collected at 20 frame per second (fps) and electron cumulative dose <10 e/^{2} (a). High magnification transmission electron micro-graphs (b) of apoferritin imaged in liquid and vitrified water.

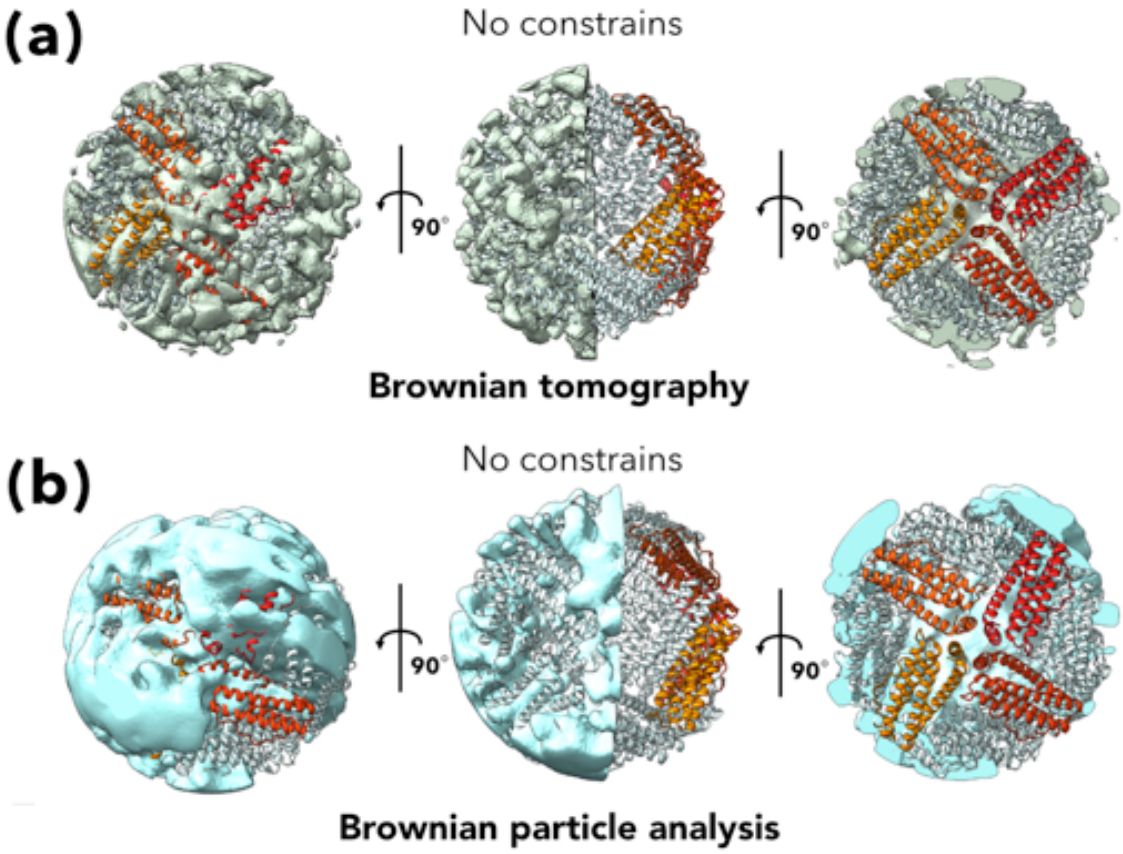

Figure S3: Brownian tomography (BT) versus Brownian particle analysis (BPA). Electron potential density (ED) maps for apoferritin generated by means of both a) BT and b) BPA using unbiased refinement, shown at different orientation.

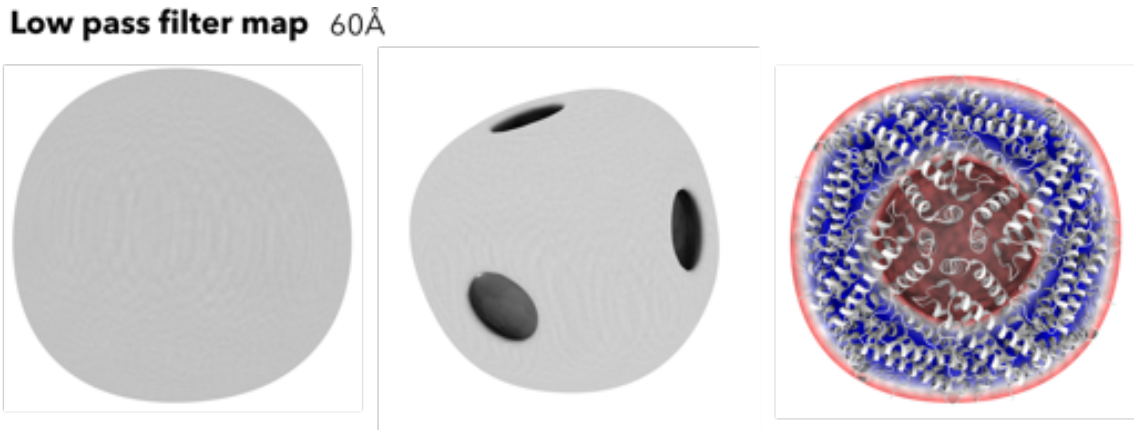

Figure S4: Low pass-filtered map of apoferritin at 60Å resolution

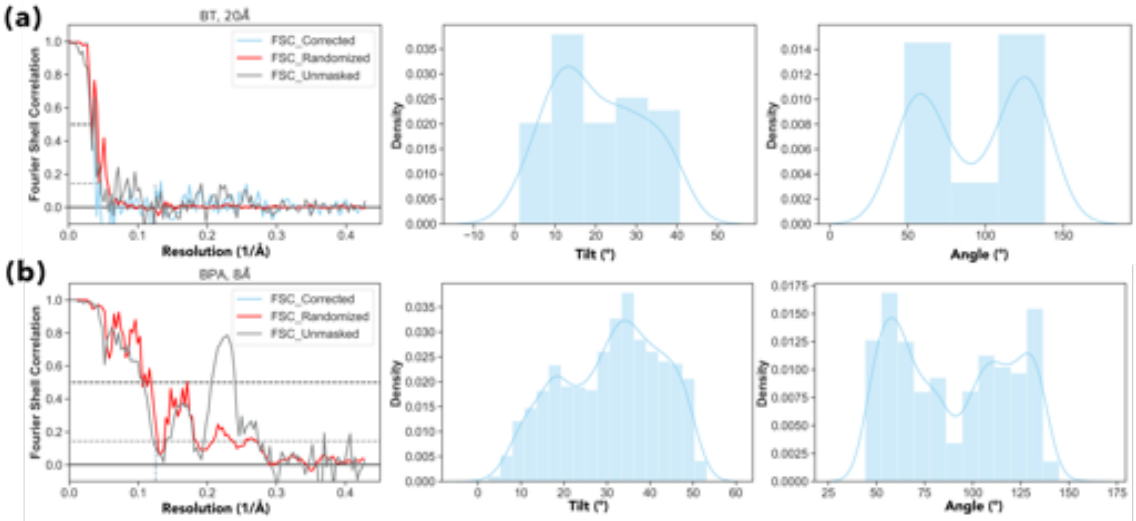

Figure S5: Fourier shell correlation and resolution assessment. For both methods, BT (a) and BPA (b), Fourier shell correlation curves calculated with RELION ([3]) are display on the left panel. Assigned tilt and angle are depicted in the middle and right panels .

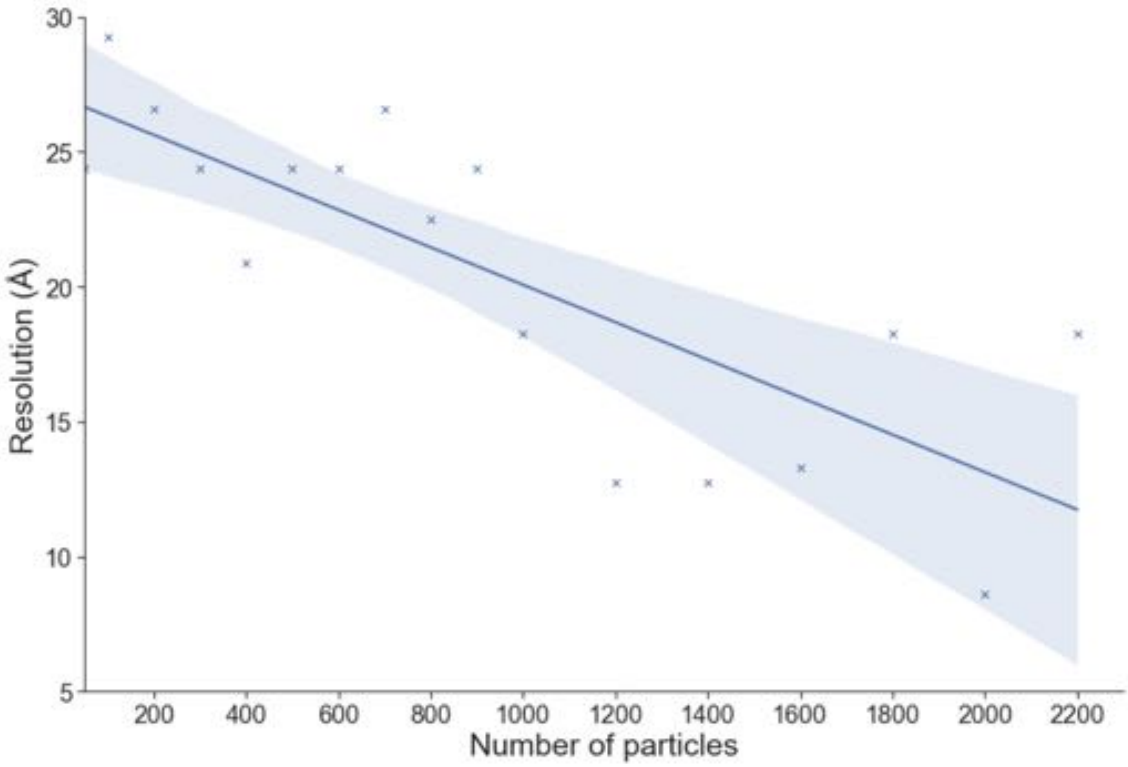

Figure S6: Reconstruction resolution vs number of profiles used. Different numbers of profiles from the video were selected from the set used from the best BPA reconstruction, these profiles were randomised. The resolution of the resulting reconstructions is shown, with the general trend showing an increase in particle number leads to an increase in resolution.

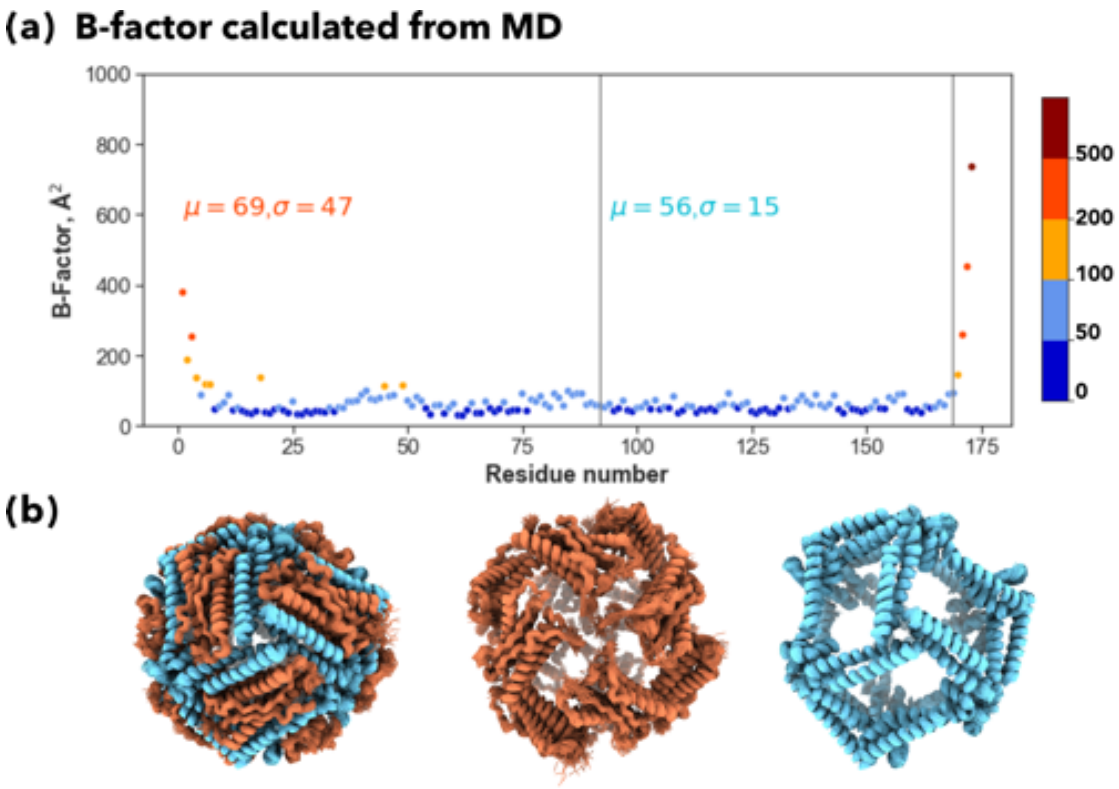

Figure S7: Apoferritin B-factor calculated from 1 μs molecular dynamics trajectory (a). Apoferritin structured coloured in orange (b-factor 69Å^2) and cyan (b-factor 56Å^2) and decomposed views

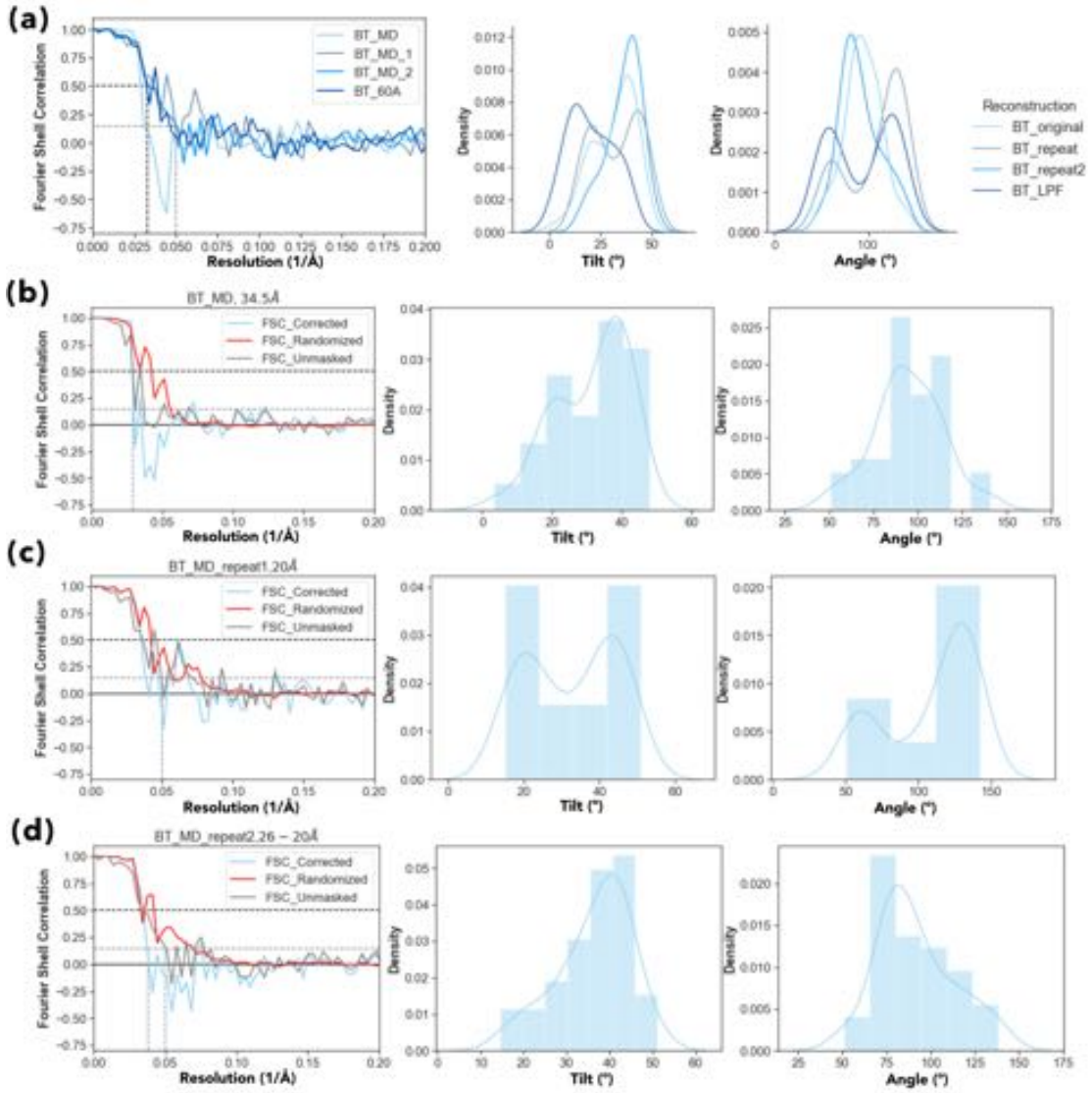

Figure S8: Fourier shell correlation and angular and tilt assignment for different BT reconstruction repeats biased with the dynamical map using the same micro-graphs dataset (a), separate panels for the three repeats are displayed in b,c,d.

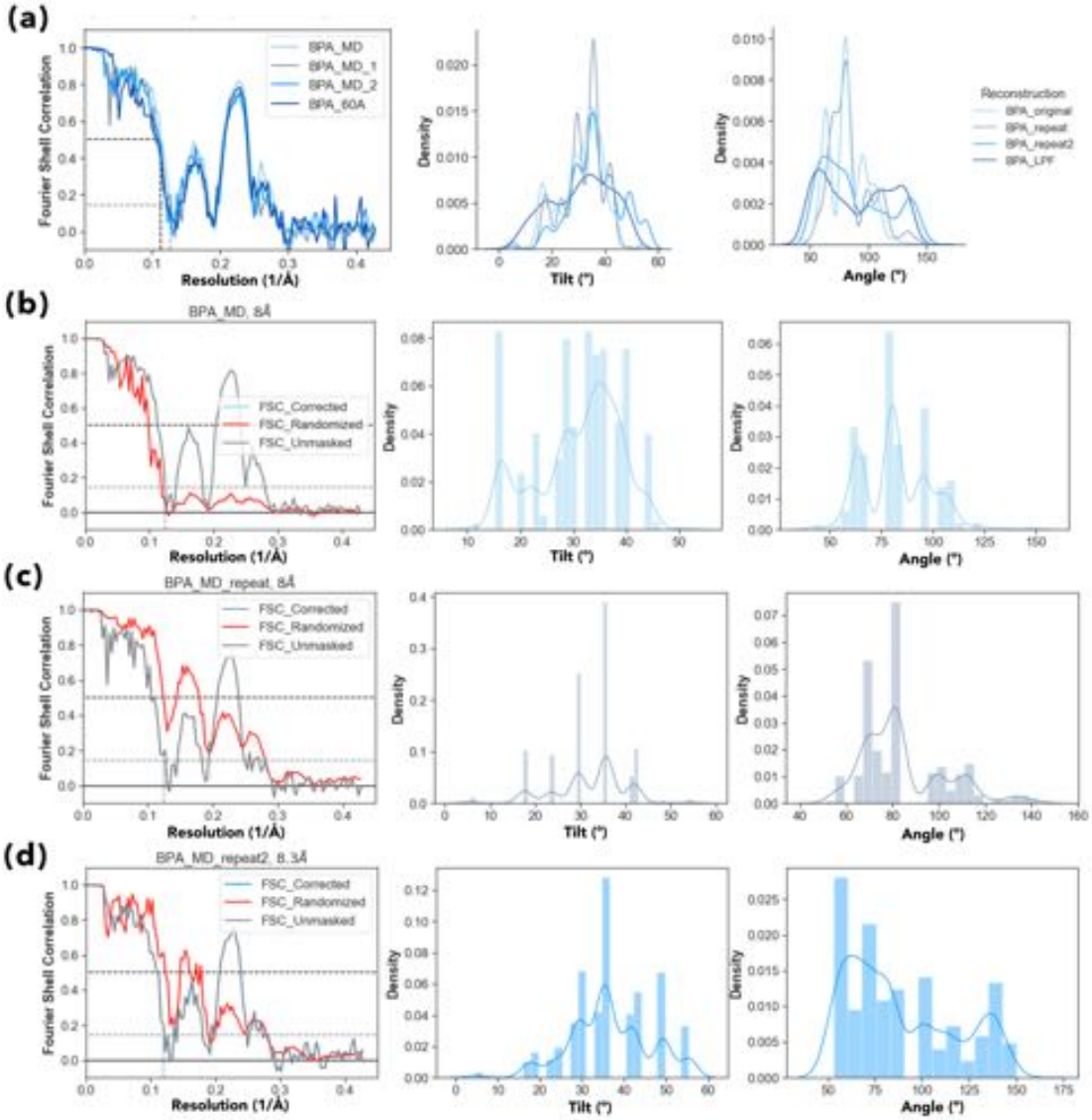

Figure S9: Fourier shell correlation and angular and tilt assignment for different BPA reconstruction repeats biased with the dynamical map using the same micro-graphs dataset (a), separate panels for the three repeats are displayed in b,c,d.

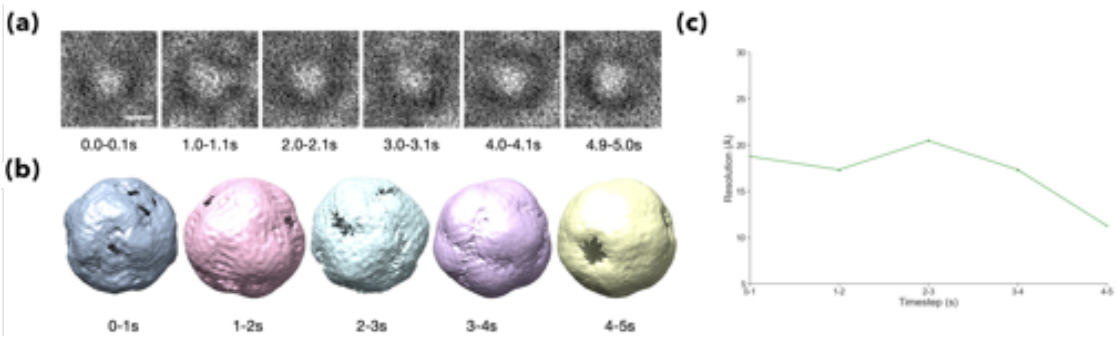

Figure S10: Time resolved reconstructions. (a) Single frame crops of an individual particle by time. (b) Resolution of time resolved reconstructions. 49 particles in the field of view were picked from every video frame, these were then reconstructed in groups of 10 frames (490 profiles), the results are shown here. (c) Resolution of Reconstructions described in (b) The resolution surprisingly decreases over time, showing there has not been significant electron damage at the resolutions visible in our reconstructions.

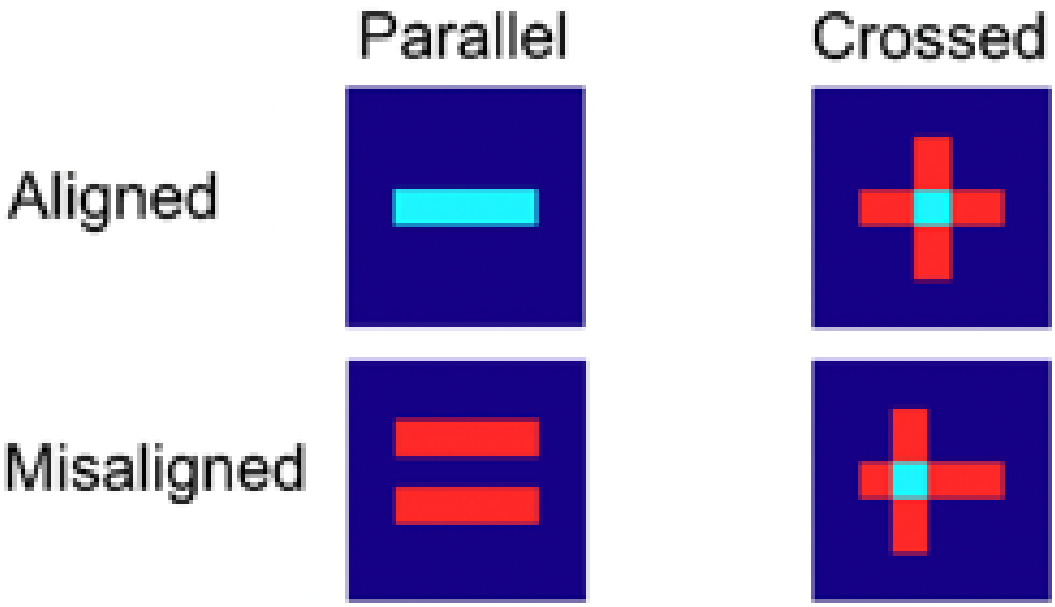

Figure S11: Schematic representation of chip position as parallel (left) or crossed (right) configurations and either aligned (top) or misaligned (bottom). In light blue the viewing window of the SiN chip where electrons are transmitted through (windows found in bottom and top chips), while in red the section of the chip where electrons are not transmitted through.

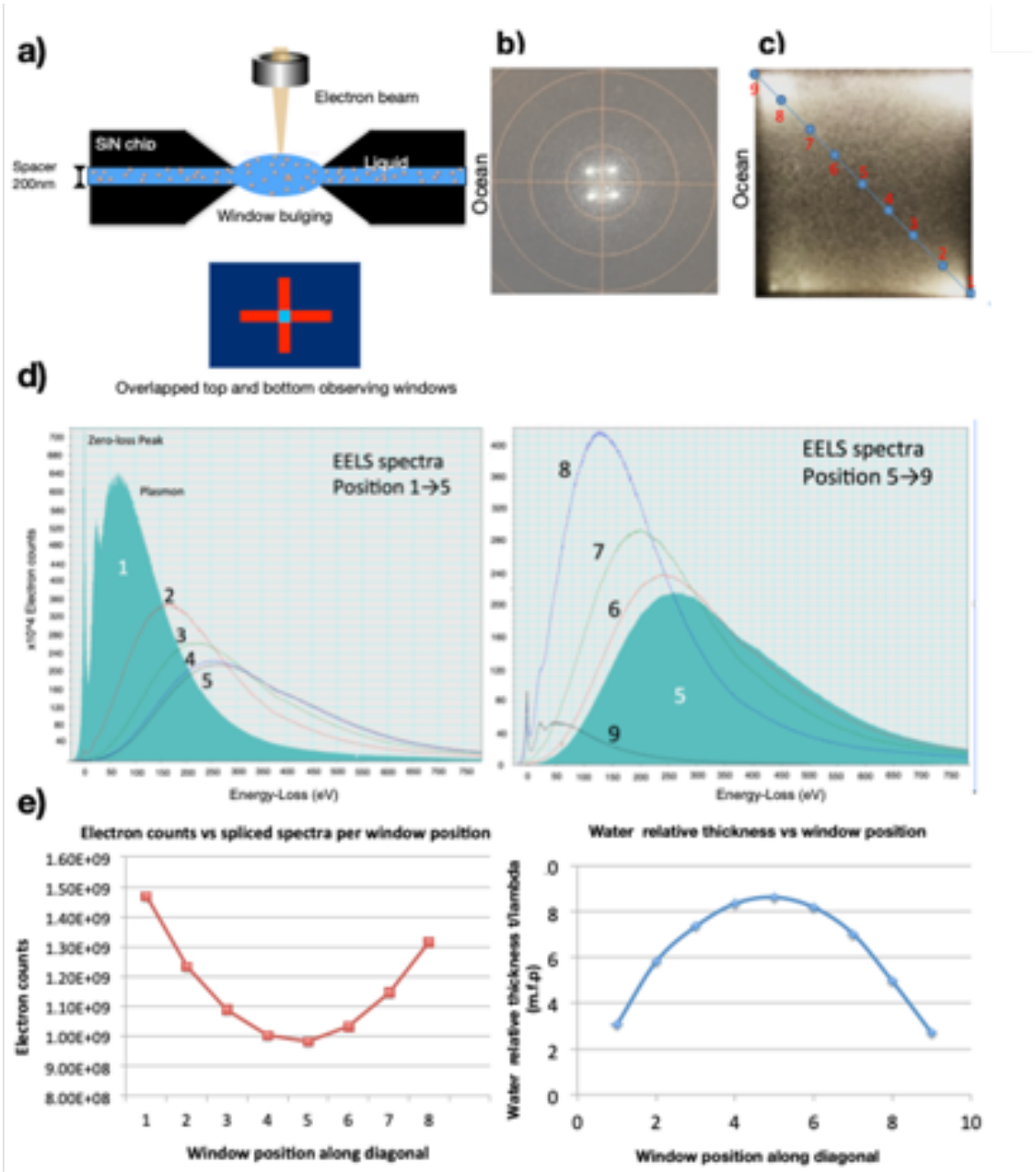

Figure S12: Investigations on sample thickness for the Ocean system via analytical TEM methods. (a) Schematic diagram of window bulging on the Ocean system when inserted into the microscope (top) and detail of windows configuration in perpendicular arrangement (bottom); (b) observing window (Ocean system) filled with liquid sample showing the dark thick and bright thin regions (c) and detailed observing window for the Ocean system marked at different positions along the diagonal for EELS study. (d) EELS spectra acquired at the positions 1 to 9 along the diagonal line (c) depicted on the Ocean window; (e) graph showing the electron counts collected by the K2 detector as a function of window position for the Ocean configurations. Water relative thickness as t/lambda m.f.p as a function of window position for the Ocean.